

FLUID FLOW CHANNELING AND MASS TRANSPORT WITH DISCONTINUOUS POROSITY DISTRIBUTION

SIMON BOISSERÉE^{1,*}, EVANGELOS MOULAS², AND MARKUS BACHMAYR¹

ABSTRACT. The flow of fluids within porous rocks is an important process with numerous applications in Earth sciences. Modeling the compaction-driven fluid flow requires the solution of coupled nonlinear partial differential equations that account for the fluid flow and the solid deformation within the porous medium. Despite the nonlinear relation of porosity and permeability that is commonly encountered, natural data show evidence of channelized fluid flow in rocks that have an overall layered structure. Layers of different rock types routinely have discontinuous hydraulic and mechanical properties. We present numerical results obtained by a novel space-time method which can handle discontinuous initial porosity (and permeability) distributions. The space-time method enables a straightforward coupling to models of mass transport for trace elements. Our results show the influence of different kinds of layering in the development of fluid-rich channels and mass transport.

1. INTRODUCTION

The flow of fluids in the Earth's subsurface is important for many applications. Examples of such applications include, but are not limited to, the migration of magma [3, 13], the flow of glaciers [6], the integrity of subsurface reservoirs [16, 33], and the efficiency of geothermal systems [28]. A distinctive aspect of the fluid flow within the deep Earth is that rocks cannot be treated as purely elastic or rigid, requiring consideration of their bulk (volumetric) viscous deformation [13, 22]. In fact, recent experiments have confirmed that the viscous/viscoelastic behavior of rocks can be observed also at near-surface conditions [20]. Thus, the volumetric deformation and the associated fluid flow need to be considered in a coupled fashion since (de)compaction can drive fluid flow and vice versa [4, 29]. In the latter studies, *porosity waves* were observed numerically. Such waves reflect the propagation of porosity perturbations (and the associated volumetric deformation) in a wave-like fashion with minimal dissipation. The transport of fluid-filled porosity in a non-dissipative fashion has been at the focus of research by geoscientists since it has important implications for the geochemical anomalies that are observed near the surface of the Earth [11, 14, 19].

The shape of porosity waves has been shown to depend very sensitively on the nonlinear behavior of the bulk (volumetric) viscosity. For example, in cases where the compaction/decompaction behavior is associated with significant changes in the effective viscosity, porosity waves take a channel-like shape (in two or three dimensions) that is responsible for the focusing of the flow

¹ INSTITUT FÜR GEOMETRIE UND PRAKTISCHE MATHEMATIK, RWTH AACHEN UNIVERSITY, TEMPLERGRABEN 55, 52056 AACHEN, GERMANY, ² INSTITUTE OF GEOSCIENCES, JOHANNES GUTENBERG-UNIVERSITÄT MAINZ, J.-J.-BECHER-WEG 21, 55128 MAINZ, GERMANY.

E-mail addresses: boisseree@igpm.rwth-aachen.de, evmoulas@uni-mainz.de, bachmayr@igpm.rwth-aachen.de.

Date: November 22, 2024.

* Author to whom any correspondence should be addressed.

S.B. has been funded in part by the German Research Foundation (DFG) – project number 442047500 – SFB 1481. E.M. would like to acknowledge the German Research Foundation (DFG) – project number 521637679 for financial support. M.B. acknowledges support by the German Research Foundation (DFG) – project number 442047500 – SFB 1481.

towards the Earth’s surface [5, 15, 16, 17, 30, 31, 32]. The focusing of the flow produces “chimney-like” features that resemble geophysical observations [16, 32]. The occurrence of such features is very important in the quantification of fluid flow and the associated geochemical anomalies [24].

An essential feature of geological formations is that rocks are typically found in layers (strata). The layers are often composed of rock types that have different physical properties, such as porosity and permeability. It is exactly this change in permeability that is responsible for the formation of geological reservoirs. For example, a typical underground reservoir must be composed of rocks of high porosity (and permeability) and must be covered by rocks of negligible porosity (and permeability) that act as a “seal” to the underlying rock units. This configuration typically requires the consideration of porosity (and permeability) jump discontinuities across the lithological boundaries. However, the methods used to solve the respective poro-viscoelastic equations numerically cannot handle a discontinuous initial porosity, and hence only approximate it by a continuous function with steep gradient. This approach leads to smoothing effects and does not preserve the discontinuous nature of solutions. Resolving the solution behavior next to a discontinuity is crucial in all the applications where the quantification of the fluid flow is needed and can thus be important for safety analyses in geoenvironmental applications [33].

Here, we consider a poro-viscoelastic model that generalizes the one introduced in [4, 29] for the interaction of porosity and pressure. For modeling sharp transitions between materials, as caused, for example, by stacked rock layers, it is important to be able to treat porosities with *jump discontinuities*. These discontinuities turn out to be determined mainly by the initial condition, as it was shown in [2] based on results from [23] for smooth initial porosities. In addition, we utilize a newly-developed space-time method that has been shown to be more accurate in solving this particular problem in the presence of jump discontinuities [1]. Our approach can be used to benchmark methods that do not include discontinuities and quantify the error between the two approaches. An additional advantage of the space-time method is that it can be coupled to simple models of chemical-tracer transport [11, 19] in a straightforward manner. The results obtained from this coupling allow us to investigate the evolution of chemical anomalies in the presence of channelized fluid flow. In particular, our results are relevant to the formation of ore deposits and to the transport of trace elements in the subsurface.

1.1. The governing equations. The model for poro-viscoelastic flow on which we focus in this work reads

$$\partial_t \phi = -(1 - \phi) \left(\phi^m \frac{p}{\sigma(p)} + Q \partial_t p \right), \quad (1a)$$

$$\partial_t p = \frac{1}{Q} \left(\nabla \cdot \frac{k_b}{\mu \phi_b^n} \phi^n (\nabla p + (1 - \phi) \delta \rho g \vec{e}_d) - \phi^m \frac{p}{\eta_b \sigma(p)} \right), \quad (1b)$$

where ϕ is the porosity (void ratio), p is the effective pressure, σ accounts for *decompaction weakening* [15, 16], Q is the compressibility (equal to K^{-1} , where K is the bulk modulus), $\delta \rho = \rho^s - \rho^f$ the density difference, and $\frac{\eta_b \sigma}{(1 - \phi) \phi^m}$ can be regarded as effective viscosity similar to [27]. Finally, t is time and \vec{e}_d is the vector indicating the gravity acceleration direction (all symbols and the respective units are given in Table 1). The problem is furthermore supplemented with initial porosity $\phi_0: \Omega \rightarrow (0, 1)$ and initial effective pressure $p_0: \Omega \rightarrow \mathbb{R}$.

An extension of the hydro-mechanical model (1) is to consider the transport of a chemical tracer (such as a trace element) as described in [11, Sec. 3]. The amount of tracer is quantified using the total concentration

$$\mathcal{C} := \phi \rho^f \chi^f + (1 - \phi) \rho^s \chi^s,$$

and fulfills the transport equation

$$\partial_t \mathcal{C} + \nabla \cdot (\mathbf{v}^e \mathcal{C}) = 0. \quad (2)$$

Symbol	Meaning	Unit	Value
ϕ	porosity		
ϕ_b	background porosity		10^{-3}
p	effective pressure	Pa	
\mathcal{C}	total concentration	$\text{kg} \cdot \text{m}^{-3}$	
η_b	bulk viscosity	$\text{Pa} \cdot \text{s}$	10^{19}
K	bulk modulus	Pa	$3 \cdot 10^9$
k_b/μ	permeability over fluid viscosity	$\text{m}^2 \cdot \text{Pa}^{-1} \cdot \text{s}^{-1}$	10^{-17}
n	Carman-Kozeny exponent		3
m	viscosity exponent		2
g	gravity	$\text{m} \cdot \text{s}^{-2}$	10
ρ^f	fluid density	$\text{kg} \cdot \text{m}^{-3}$	2500
ρ^s	solid density	$\text{kg} \cdot \text{m}^{-3}$	3000
χ^f	fluid mass fraction		
χ^s	solid mass fraction		
K_D	concentration ratio $\frac{\rho^s \chi^s}{\rho^f \chi^f}$		10^{-3}
\mathbf{v}^f	fluid velocity	$\text{m} \cdot \text{s}^{-1}$	
\mathbf{v}^s	solid velocity	$\text{m} \cdot \text{s}^{-1}$	

TABLE 1. Variables and physical quantities

Here \mathbf{v}^e denotes the effective velocity and at the limit where $\mathbf{v}^s \approx 0$ holds, is given by

$$\mathbf{v}^e = \frac{\mathbf{v}^f \phi}{\phi + (1 - \phi)K_D}, \quad \mathbf{v}^f = \frac{1}{\phi} \frac{k_b}{\mu \phi_b^n} \phi^n (\nabla p + (1 - \phi) \delta \rho g \vec{e}_d),$$

where $K_D = \frac{\rho^s \chi^s}{\rho^f \chi^f}$ describes the concentration ratio of the tracer which is assumed to be constant as already indicated in Table 1. The specific form of (2) is valid at the limit where grain-scale chemical diffusion and hydro-dynamic dispersion are ignored. Previous studies indicate that, at the large scales considered here, these phenomena can be neglected [19, 26].

1.2. Existing numerical methods. Various methods have been proposed to solve the above type of problem numerically, for example finite difference schemes with implicit time-stepping in [4] and adaptive wavelets in [29]. In a number of recent works, pseudo-transient schemes based on explicit time stepping in a pseudo-time variable have been investigated. Due to their compact stencils, low communication overhead and simple implementation, such schemes are well suited for parallel computing on GPUs, so that very high grid resolutions can be achieved to compensate the low order of convergence, as shown for example in [15, 16, 17, 18, 28, 32]. Even though all of these schemes are observed to work well for smooth initial porosities ϕ_0 , their convergence can be very slow in problems with non-smooth ϕ_0 , in particular in the presence of discontinuities [1]. In such cases, due to the smoothing that is implicit in the finite difference schemes, accurately resolving sharp localized features can require extremely large grids.

1.3. Novel contributions. We solve the hydro-mechanical (HM) problem given by (1) using the space-time adaptive method introduced in [1]. This approach can handle discontinuities in the porosity ϕ without approximating it by a continuous function with steep gradient. As a result, smaller grids and less computational effort are needed compared to continuous schemes such as finite differences. Since the method generates efficient approximations of the entire time history of a solution to (1) in a sparse format, its coupling to the problem of chemical-tracer transport (CT) given by (2) becomes straightforward. This is because the CT problem does not give feedback to the model (1), and thus solving it can be seen as post-processing step.

1.4. Outline. Since our results from the HM model (1) are uncoupled to the results of the CT problem (2), we begin with a short description of the methods used to solve the HM model. In Section 2 we introduce the methods to obtain the numerical results both for the HM model in Section 3 and for the CT problem in Section 4. We finish with a discussion regarding the implication of our results for the porous fluid transport in natural systems.

2. METHODS

2.1. Hydro-mechanical model (HM). To solve (1) we consider the space-time adaptive method which was introduced in [1] based on a combination of a Picard iterations for (1a) and a particular adaptive least squares discretization of (1b) which itself is based on [7, 8, 9]. To make this more precise we start by introducing the new variable $\varphi = -\log(1 - \phi)$, so that $\phi = 1 - e^{-\varphi}$, because then the system (1) can be written in the form

$$\partial_t \varphi = - \left(\beta(\varphi) \frac{p}{\sigma(p)} + Q \partial_t p \right), \quad (3a)$$

$$\partial_t p = \frac{1}{Q} \left(\nabla \cdot \alpha(\varphi) (\nabla p + \zeta(\varphi)) - \beta(\varphi) \frac{p}{\sigma(p)} \right), \quad (3b)$$

where

$$\alpha(\varphi) := \frac{k_b}{\mu \phi_b^n} (1 - e^{-\varphi})^n, \quad \beta(\varphi) := \frac{1}{\eta_b} (1 - e^{-\varphi})^m, \quad \zeta(\varphi) := e^{-\varphi} \delta \rho g \vec{e}_d.$$

To solve (3b) for a fixed $\bar{\varphi}$ we consider a linearization, that is, we solve

$$\partial_t p^{(k)} = \frac{1}{Q} \left(\nabla \cdot \alpha(\bar{\varphi}) (\nabla p^{(k)} + \zeta(\bar{\varphi})) - \beta(\bar{\varphi}) \frac{p^{(k)}}{\sigma(p^{(k-1)})} \right), \quad (4)$$

for $p^{(k)}$ given the previous iterate $p^{(k-1)}$. By defining

$$G[\bar{p}](p, \psi) := \begin{pmatrix} \frac{1}{Q} (\operatorname{div}(p, \psi) + \beta(\bar{\varphi}) \frac{p}{\sigma(\bar{p})}) \\ \psi + \alpha(\bar{\varphi}) \nabla_x p \\ p(0, \cdot) \end{pmatrix}, \quad R := \begin{pmatrix} 0 \\ -\alpha(\bar{\varphi}) \zeta(\bar{\varphi}) \\ p_0 \end{pmatrix},$$

with $\operatorname{div}(p, \psi) := \partial_t p + \operatorname{div}_x \psi$ we can reformulate (4) as first-order system

$$G[p^{(k-1)}](p^{(k)}, \psi^{(k)}) = R. \quad (5)$$

Numerically we now use the approach presented in [7, 8, 9], and thus calculate a least squares minimizer with respect to an appropriately chosen norm. Using the numerical approximation of $p[\bar{\varphi}]$ from (5) we solve (3a) by discretizing the iteration

$$\varphi^{(k+1)}(t, \cdot) = Q(p_0 - p[\varphi^{(k)}](t, \cdot)) - \int_0^t \beta(\varphi^{(k)}) \frac{p[\varphi^{(k)}](s, \cdot)}{\sigma(p[\varphi^{(k)}](s, \cdot))} ds.$$

which is based on integrating (3a) in time. For more details including proofs of convergence we refer to [1, Sec. 3, 4].

The resulting adaptive scheme yields efficient approximations of localized features of solutions, in particular in the presence of discontinuities. In addition, this scheme can generate space-time grids corresponding to spatially adapted time steps; an example of this can be found in Figure 1. The method provides computable *a-posteriori* estimates of the error with respect to the exact solution of the coupled nonlinear system (3). Furthermore, one obtains optimal convergence rates for ϕ and p independent of the presence of discontinuities in ϕ , as observed in [1, Sec. 5.2].

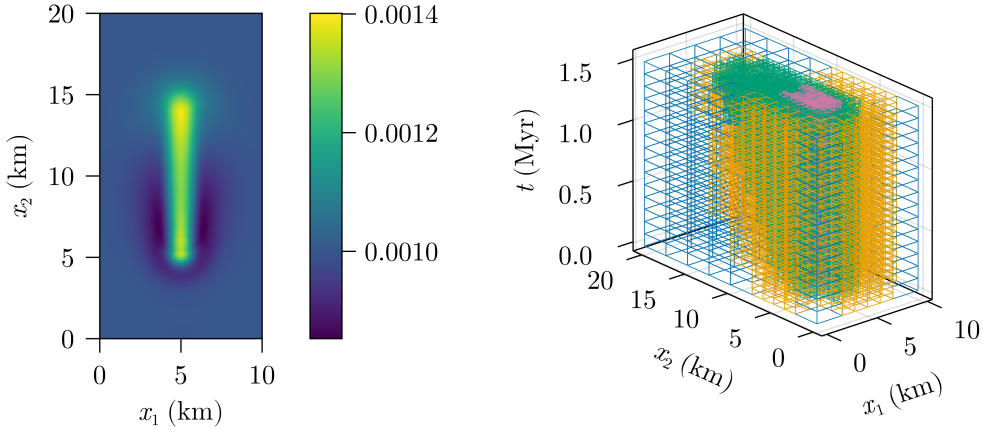


FIGURE 1. Example of a porosity channel at $t = 1.5$ (Myr) on the left with the associated adaptive space-time grid on the right

2.2. Chemical-tracer transport model (CT). To solve the chemical transport equation (2), we follow its characteristics for many different starting values using an explicit Euler scheme. Note that this approach is highly parallelizable, since we need to solve a high number of independent ODEs for each starting value. By exploiting this we usually achieve very low wall-clock times, even for many starting values corresponding to a high resolution.

2.3. Model parameters. The model parameters can be derived by non-dimensionalizing the physical models (1) and (2) with values given in Table 1. Using x (10^4 m), $\delta\rho g$ and η_b as independent scales reduces our model parameters to

$$Q = \frac{1}{60}, \quad \eta_b = 1, \quad \frac{k_b}{\mu\phi_b^n} = 1000, \quad \delta\rho g \vec{e}_d = \begin{pmatrix} 0 \\ 1 \end{pmatrix}.$$

Furthermore, we consider σ , as suggested in [15, 16], which is an expression of the form

$$\begin{aligned} \sigma(v) &= 1 - \frac{1 - c_1}{2} \left(1 + \tanh\left(-\frac{v}{c_2}\right) \right) \\ &= \frac{c_1 + \exp(2v/c_2)}{1 + \exp(2v/c_2)}, \quad v \in \mathbb{R}, \end{aligned} \quad (6)$$

and provides a phenomenological model for decompaction weakening. Here $c_1 \in (0, 1]$ and $c_2 > 0$, where $1 + \tanh$ can be regarded as a smooth approximation of a step function taking values in the interval $(0, 2)$. In the most well-studied case $c_1 = 1$, as considered in [29], one observes the formation of porosity waves, whereas the case of $c_1 < 1$ with appropriate problem parameters and initial conditions, one can observe the formation of channels. With parameters from the stated ranges, σ as in (6) fulfills [2, Assumptions 1], and hence we refer to [2, Sec. 4] for the well-posedness of (1).

In this work we consider two cases, namely $c_1, c_2 = 1$ (no decompaction weakening) and $c_1, c_2 = 0.002$ (including decompaction weakening). The resulting functions read

$$\sigma^a(v) = 1, \quad \sigma^b(v) = \frac{0.002 + \exp(1000v)}{1 + \exp(1000v)}, \quad v \in \mathbb{R}.$$

3. HYDRO-MECHANICAL MODEL RESULTS

In this part we show numerical results for solving (1) using the method described in Section 2.1. We compare three different initial porosities which are shown in Figure 2, reflecting our main focus on investigating the cases of jump discontinuities in the initial porosity distribution. Taking an initial homogeneous porosity as a reference case (left panel of Figure 2), we consider a drop

(middle panel of Figure 2) versus an increase (right panel of Figure 2) in the initial porosity distribution. For the effective pressure p , we assume homogeneous initial data $p_0(x) = 0$.

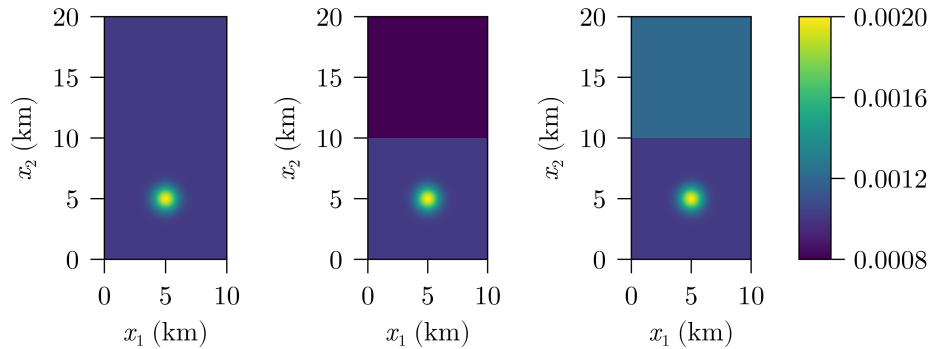


FIGURE 2. Three initial porosity distributions ϕ_0^a , ϕ_0^b and ϕ_0^c (from left to right)

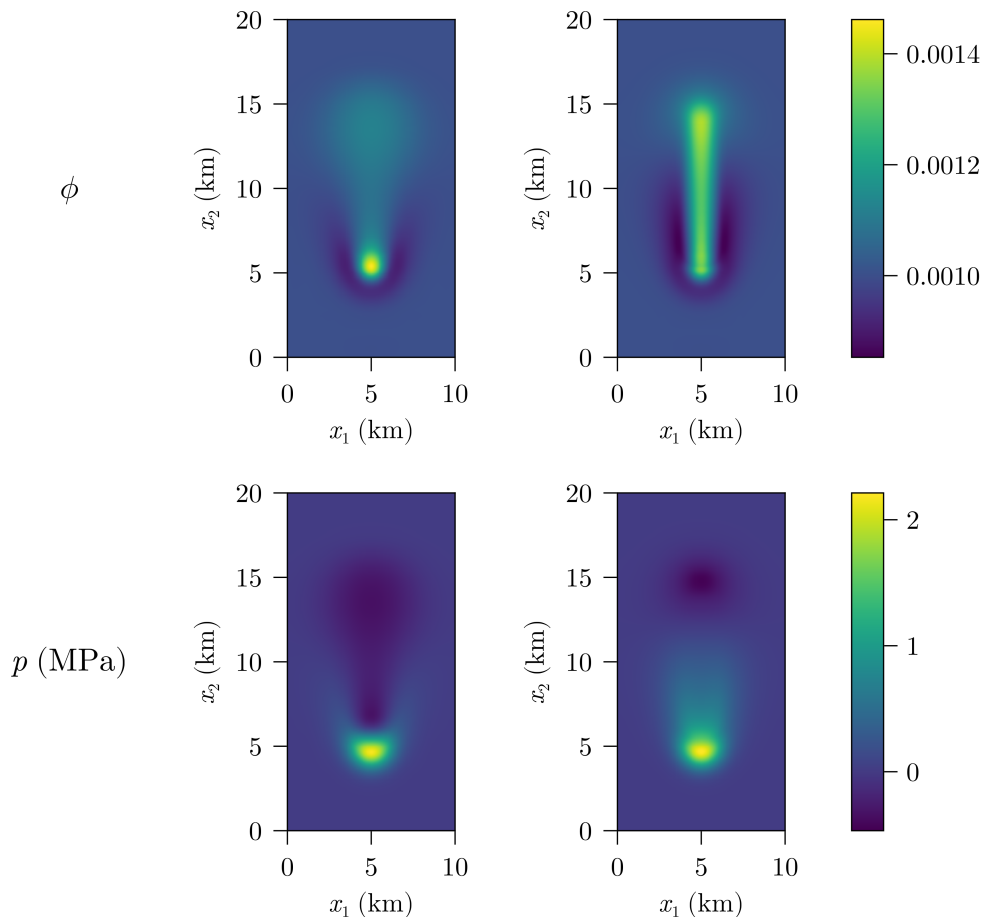


FIGURE 3. Porosity and effective pressure after $T = 1.5$ Myr for ϕ_0^a with σ^a (left) and with σ^b (right)

We start with the well-known scenario of the smooth initial porosity ϕ_0^a as in Figure 2 (left) and compare the results without decompaction weakening (σ^a) and with decompaction weakening (σ^b) in Figure 3. The resulting plots show the expected spreading of the fluid front in the case without decompaction weakening in the left panel of Figure 3. In contrast, the fluid flow is focused in the presence of weakening as one can see in the right panel of Figure 3.

These results are used as reference and will not be discussed further since they confirm previous findings [4, 5, 16, 31].

Figure 4 shows the results of the two initial conditions ϕ_0^b and ϕ_0^c from Figure 2 (middle, right) that consider an initial porosity discontinuity. Both results consider the case without

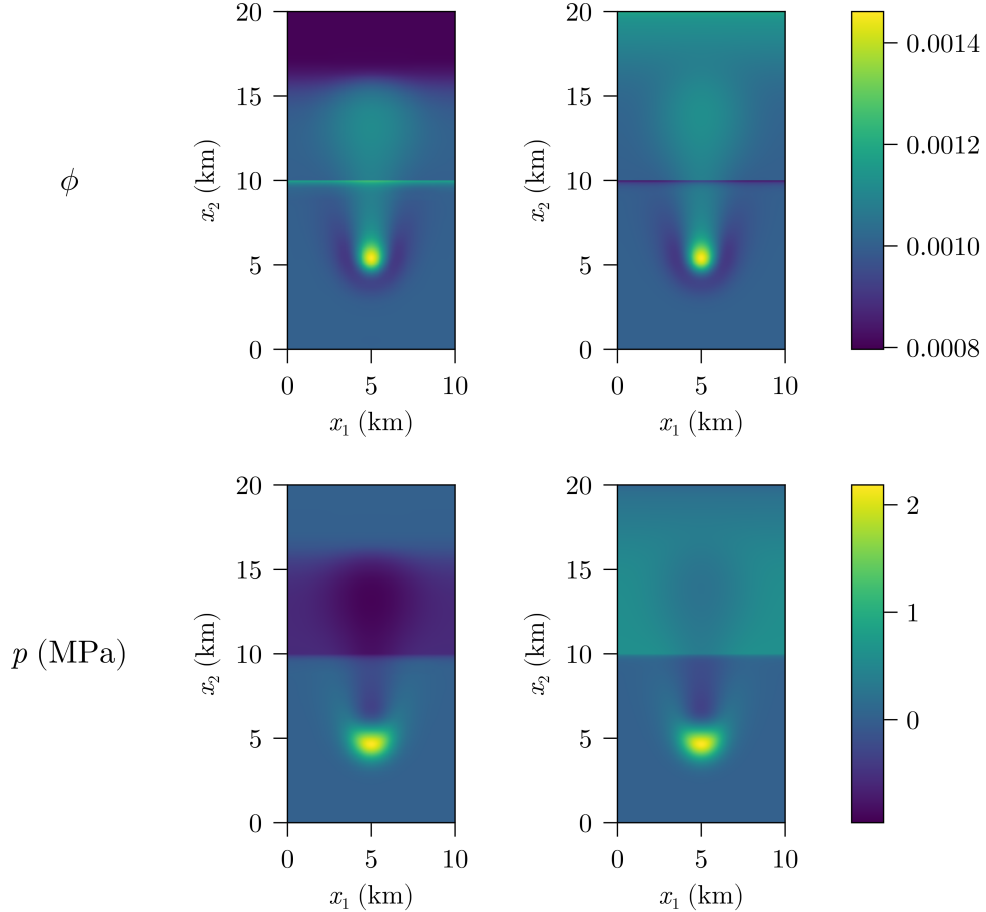
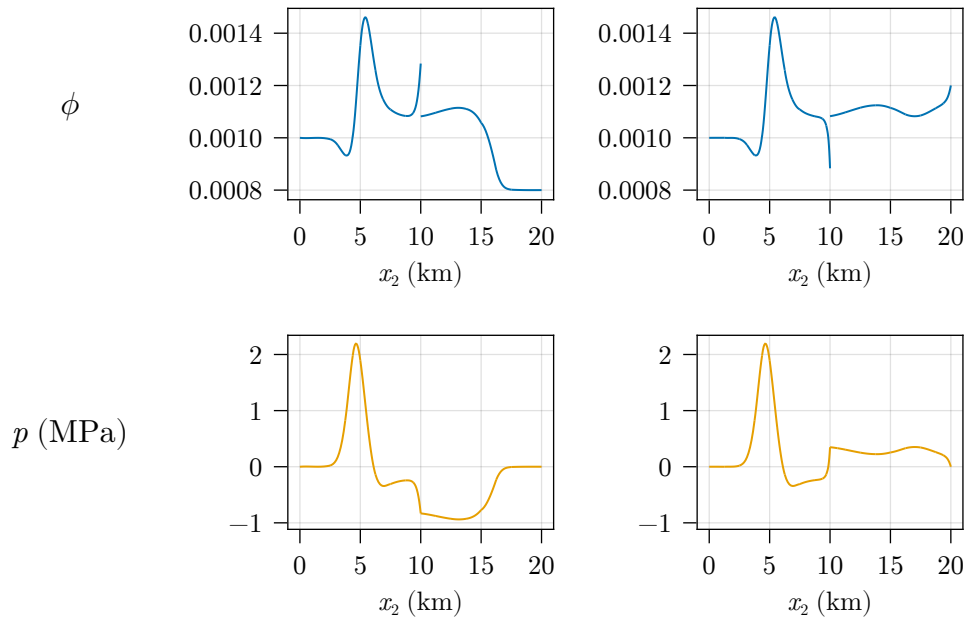
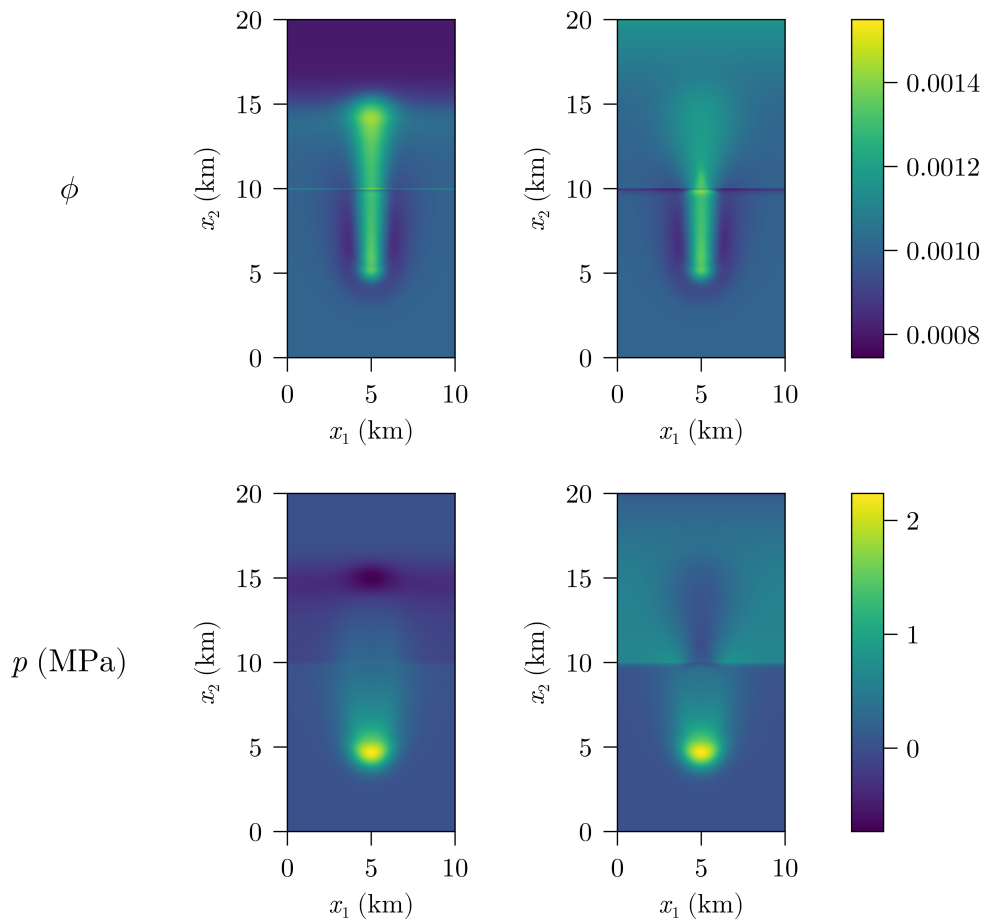


FIGURE 4. Porosity and effective pressure after $T = 1.5$ Myr for ϕ_0^b (left) and ϕ_0^c (right) with σ^a

decompaction weakening. One can see very sharp transitions of ϕ at the locations of the initial discontinuities. As it is especially visible for the porosity distribution, the sign of its transition (positive or negative) depends on whether the initial porosity of the upper layer was smaller (negative jump) or larger (positive jump) compared to the porosity of the underlying layer. Figure 5 shows a cross section of Figure 4 that shows the discontinuities in ϕ more clearly. In contrast, the solution for p is continuous which aligns with the theory derived in [2, Sec. 4].

Figure 6 shows the effect of decompaction weakening on the same initial discontinuous configurations (case σ^b). In the case of the negative jump (ϕ_0^b), the channel has a slightly higher maximal porosity compared to the continuous case. Furthermore, Figure 6 (left) shows that there is a very steep increase in porosity at the place of the discontinuity. On the other hand, for the positive jump (ϕ_0^c), the channel focuses significantly before spreading in the high-porosity/permeability zone as it is shown in the right panel of Figure 6. This can be expected: we see a narrower channel in the less porous domain, but it spreads quickly once the fluid enters the domain of high porosity and permeability. This shows that the fluid does not need to channelize as much as in the less porous domain in order to travel upwards.

FIGURE 5. Cross section of Figure 4 for $x_1 = 5$ kmFIGURE 6. Porosity and effective pressure after $T = 1.5$ Myr for ϕ_0^b (left) and ϕ_0^c (right) with σ^b

4. CHEMICAL-TRANSPORT MODEL RESULTS

An extension of the general model (1) is to consider the transport of a chemical tracer by solving (2). This is achieved by following its characteristics as described in Section 2.2. The natural range of partition coefficients can be very large [10] and their magnitudes depend on several parameters [12]. Without loss of generality, we examine the ratio $K_D = 10^{-3}$ (as already indicated in Table 1) to consider incompatible elements. Incompatible elements are those that partition preferentially in the fluid. Solving for \mathcal{C} and using the prescribed values for ρ^s , ρ^f and K_D from Table 1 directly yields χ^s and χ^f as well.

In this part, we will only plot the normalized chemical tracer $\mathcal{C}/\mathcal{C}_0$. For simplicity, we consider constant initial data $\mathcal{C}_0(x) = 1$ since \mathcal{C} in (2) can be scaled arbitrarily without affecting the solution.

Figure 7 shows the normalized tracer compositions $\mathcal{C}/\mathcal{C}_0$ connected to the solutions shown in Figure 3 (with ϕ_0^a) for $K_D = 10^{-3}$. We see the distribution of an incompatible element

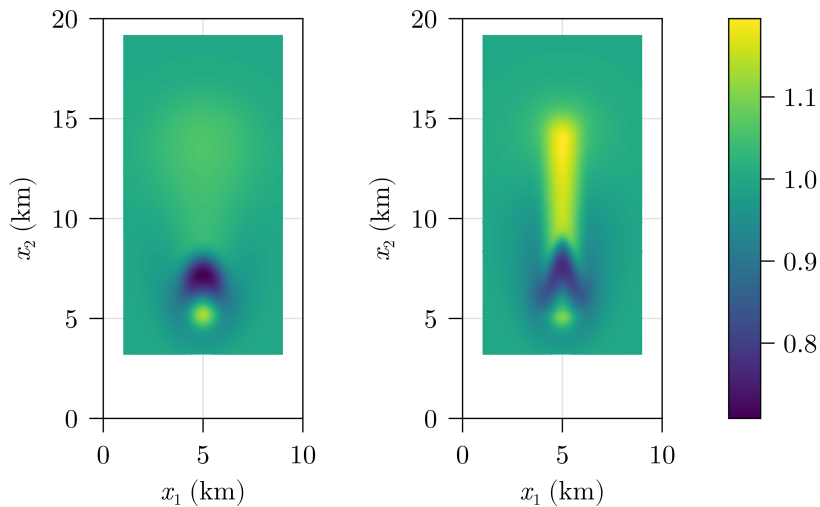


FIGURE 7. $\mathcal{C}/\mathcal{C}_0$ after $T = 1.5$ Myr for an initially continuous porosity (ϕ_0^a) and for the cases without decompaction weakening (σ^a ; left) and with decompaction weakening (σ^b ; right)

that prefers to stay with the fluid, and hence, it gets transported efficiently while draining the area of origin. The role of decompaction weakening becomes more apparent in the case the channelization of the fluid flow as shown in Figure 7 (right panel). In that case, we observe a more pronounced enrichment in the region defined by the fluid-rich channel. It is important to note that this enrichment occurs in both the solid and the fluid, and it occurs at the expense of the trace element's distribution in the source region.

The solution of the CT problem having initial discontinuous porosity ϕ_0 is shown in Figure 8. This figure is calculated based on the HM model (porosity-pressure evolution) shown in Figure 4 and assumes no decompaction weakening (σ^a). The results generally agree with the previous findings that show that the incompatible elements ($K_D = 10^{-3}$) travel further and enrich the upper layer. Furthermore, this enrichment seems to be traveling slightly faster in the region where the initial fluid content was higher (central region of the domain). This requires that the propagation velocity of the enrichment front is not constant and moves further from the location of the porosity discontinuity, which is located exactly at the middle of the domain ($x_2 = 10$ km). However, the enrichment is more pronounced in the case of a negative porosity jump (case ϕ_0^b) compared to the case of positive porosity jump (ϕ_0^c).

Finally, Figure 9 shows the resulting normalized tracer element $\mathcal{C}/\mathcal{C}_0$ for the case of decompaction weakening (σ^b) and an initially discontinuous porosity ϕ_0 . The associated HM model

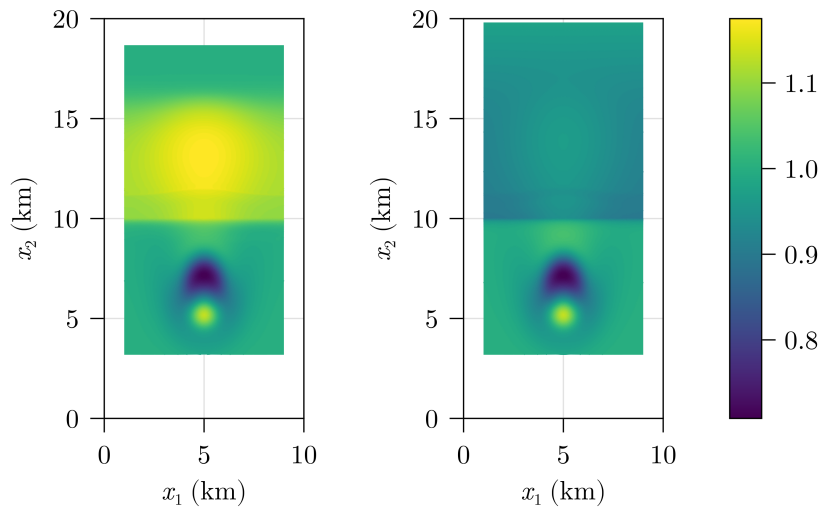


FIGURE 8. C/C_0 after $T = 1.5$ Myr for ϕ_0^b (left) and ϕ_0^c (right) with σ^a

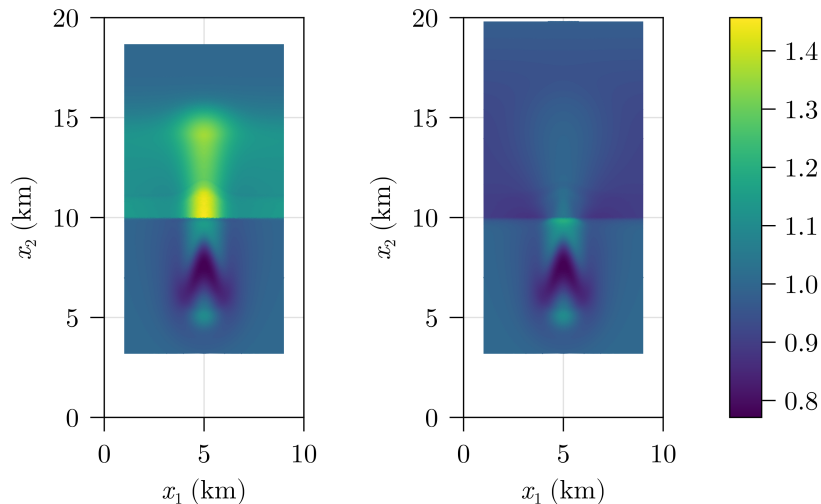


FIGURE 9. C/C_0 after $T = 1.5$ Myr for ϕ_0^b (left) and ϕ_0^c (right) with σ^b

can be found in Figure 6. The resulting cases show marked differences and can be summarized as follows. The case with negative jump discontinuity (ϕ_0^b) shows a marked enrichment with respect to the incompatible element. This enrichment is in general heterogeneous and it propagates further by mostly following the fluid channel. Interestingly, for the case of positive jump discontinuity (ϕ_0^c), the enrichment of the incompatible element is localized close to the discontinuity location. This is explained by the fact that the fluid spreads beyond this point as it was shown in Figure 6 (right column).

5. DISCUSSION AND CONCLUSIONS

We have presented results for the case of compaction-driven fluid flow in relation to fluid migration in the deep subsurface. Our method aims to resolve the effects of discontinuous porosity distributions as already discussed in [1]. The models confirm previous findings for the cases of homogeneous initial porosity (ϕ_0) distribution [4, 5, 16, 31]. However, for the cases when the ϕ_0 has jump discontinuities, our method predicts discontinuous solutions without artificial smoothing due to numerical diffusion. Such results are useful for cases where the mechanical

variables, such as the effective and fluid pressure, need to be quantified in applications [16,33], and thus, our approach can be used to provide a reference case for numerical benchmarks.

An additional advantage of the space-time method is that the one-way coupling of the HM problem to the CT problem can be easily solved using the pre-calculated results of the HM problem. This allows for the investigation of the behavior of various trace elements and the overall mass transport in rock formations that have discontinuous porosity. Our results confirm previous data which suggest that incompatible elements are the most mobile and can travel together with the fluid [19]. This selective enrichment in incompatible elements becomes more prominent in cases where the flow is channelized, leading to the formation of localized geochemical and mineralogical anomalies. Although such mechanisms have been discussed in previous works [21,24], the mechanism for the channeling in our case is different. In the aforementioned studies, the formation of channels was due to the selective dissolution of matrix minerals [21,25]. In contrast, in our case the channeling is the result of decompaction weakening [5,31,32]. In any case, it becomes apparent that, whatever the localization mechanism may be, the localization of the fluid amplify the enrichment of incompatible elements significantly.

The consideration of our new method in cases of initially discontinuous porosity distributions provided us with new insights with respect to the transport of incompatible elements. In particular, for the case of a negative jump discontinuity (ϕ_0^b), the discontinuity creates a chemical-enrichment front that migrates away from the location of the actual discontinuity of the HM-problem solution. Finally, it is evident from our results that the effects of the channeling of the flow together with the presence of initial discontinuities will produce a variety of element-enrichment patterns that can be investigated in future studies that focus on particular element behavior.

REFERENCES

- [1] M. Bachmayr and S. Boisserée. An adaptive space-time method for nonlinear poroviscoelastic flows with discontinuous porosities, 2024.
- [2] M. Bachmayr, S. Boisserée, and L. M. Kreusser. Analysis of nonlinear poroviscoelastic flows with discontinuous porosities. *Nonlinearity*, 36:7025–7064, 11 2023.
- [3] V. Barcion and F. M. Richter. Nonlinear waves in compacting media. *Journal of Fluid Mechanics*, 164:429–448, 1986.
- [4] J. A. D. Connolly and Y. Y. Podladchikov. Compaction-driven fluid flow in viscoelastic rock. *Geodinamica Acta*, 11(2-3):55–84, 1998.
- [5] J. A. D. Connolly and Y. Y. Podladchikov. Decompaction weakening and channeling instability in ductile porous media: Implications for asthenospheric melt segregation. *Journal of Geophysical Research: Solid Earth*, 112(B10), 2007.
- [6] A.C. Fowler. On the transport of moisture in polythermal glaciers. *Geophysical & Astrophysical Fluid Dynamics*, 28(2):99–140, 1984.
- [7] T. Führer and M. Karkulik. Space-time least-squares finite elements for parabolic equations. *Computers & Mathematics with Applications*, 92:27–36, 2021.
- [8] G. Gantner and R. Stevenson. Further results on a space-time FOSLS formulation of parabolic PDEs. *ESAIM Math. Model. Numer. Anal.*, 55(1):283–299, 2021.
- [9] G. Gantner and R. Stevenson. Improved rates for a space-time FOSLS of parabolic PDEs. *Numerische Mathematik*, 156:133–157, 2024.
- [10] A.J. Irving. A review of experimental studies of crystal/liquid trace element partitioning. *Geochimica et Cosmochimica Acta*, 42(6):743–770, 1978.
- [11] J. S. Jordan, M. A. Hesse, and J. F. Rudge. On mass transport in porosity waves. *Earth and Planetary Science Letters*, 485:65–78, 2018.
- [12] S. Karato. Physical basis of trace element partitioning: A review. *American Mineralogist*, 101(1):2577–2593, 2016.
- [13] D. McKenzie. The generation and compaction of partially molten rock. *Journal of petrology*, 25(3):713–765, 1984.
- [14] O. Navon and E. Stolper. Geochemical consequences of melt percolation: The upper mantle as a chromatographic column. *The journal of Geology*, 95(3):285–307, 1987.

- [15] L. Räss, T. Duretz, and Y. Y. Podladchikov. Resolving hydromechanical coupling in two and three dimensions: spontaneous channelling of porous fluids owing to decompaction weakening. *Geophysical Journal International*, 218(3):1591–1616, 2019.
- [16] L. Räss, N. S. C. Simon, and Y. Y. Podladchikov. Spontaneous formation of fluid escape pipes from subsurface reservoirs. *Scientific reports*, 8(1):1–11, 2018.
- [17] L. Räss, V. M. Yarushina, N. S.C. Simon, and Y. Y. Podladchikov. Chimneys, channels, pathway flow or water conducting features - an explanation from numerical modelling and implications for CO2 storage. *Energy Procedia*, 63:3761–3774, 2014.
- [18] G. S. Reuber, L. Holbach, and L. Räss. Adjoint-based inversion for porosity in shallow reservoirs using pseudo-transient solvers for non-linear hydro-mechanical processes. *Journal of Computational Physics*, 423:109797, 2020.
- [19] F.M. Richter. Simple models for trace element fractionation during melt segregation. *Earth and Planetary Science Letters*, 77(3-4):333–344, 1986.
- [20] A. Sabitova, V.M. Yarushina, S. Stanchits, V. Stukachev, L. Khakimova, and A. Myasnikov. Experimental Compaction and Dilation of Porous Rocks During Triaxial Creep and Stress Relaxation. *Rock Mechanics and Rock Engineering*, 54(11):5781–5805, 2021.
- [21] A. Schiemenz, Y. Liang, and E.M. Parmentier. A high-order numerical study of reactive dissolution in an upwelling heterogeneous mantle -I.: Channelization, channel lithology and channel geometry. *Geophysical Journal International*, 186(2):641–664, 2011.
- [22] D. R. Scott and D. J. Stevenson. Magma ascent by porous flow. *Journal of Geophysical Research: Solid Earth*, 91(B9):9283–9296, 1986.
- [23] G. Simpson, M. Spiegelman, and M. I. Weinstein. Degenerate dispersive equations arising in the study of magma dynamics. *Nonlinearity*, 20(1):21–49, 2006.
- [24] M. Spiegelman and P.B. Kelemen. Extreme chemical variability as a consequence of channelized melt transport. *Geochemistry, Geophysics, Geosystems*, 4(7):1–18, 2003.
- [25] M. Spiegelman, P.B. Kelemen, and E. Aharonov. Causes and consequences of flow organization during melt transport: The reaction infiltration instability in compactible media. *Journal of Geophysical Research: Solid Earth*, 106(B2):2061–2077, 2001.
- [26] M. Stavropoulou, P. Papanastasiou, and I. Vardoulakis. Coupled wellbore erosion and stability analysis. *Int. J. Numer. Anal. Meth. Geomech.*, 22(9):749–769, 1998.
- [27] D. J. Stevenson and D. R. Scott. Mechanics of fluid-rock systems. *Annual Review of Fluid Mechanics*, 23:305–339, 1991.
- [28] I. Utkin and A. Afanasyev. Decompaction weakening as a mechanism of fluid focusing in hydrothermal systems. *Journal of Geophysical Research: Solid Earth*, 126(9):e2021JB022397, 2021.
- [29] O. V. Vasilyev, Y. Y. Podladchikov, and D. A. Yuen. Modeling of compaction driven flow in poro-viscoelastic medium using adaptive wavelet collocation method. *Geophysical Research Letters*, 25(17):3239–3242, 1998.
- [30] V. M. Yarushina and Y. Y. Podladchikov. (De)compaction of porous viscoelastoplastic media: Model formulation. *Journal of Geophysical Research: Solid Earth*, 120(6):4146–4170, 2015.
- [31] V. M. Yarushina, Y. Y. Podladchikov, and J. A. D. Connolly. (De)compaction of porous viscoelastoplastic media: Solitary porosity waves. *Journal of Geophysical Research: Solid Earth*, 120(7):4843–4862, 2015.
- [32] V. M. Yarushina, Y. Y. Podladchikov, and L. H. Wang. Model for (de)compaction and porosity waves in porous rocks under shear stresses. *Journal of Geophysical Research: Solid Earth*, 125(8):e2020JB019683, 2020.
- [33] V. M. Yarushina, L. H. Wang, D. Connolly, G. Kocsis, I. Fæstø, S. Polteau, and A. Lakhli. Focused fluid-flow structures potentially caused by solitary porosity waves. *Geology*, 50(2):179–183, 2022.